Title:

Fast X-Ray Tomography for the Quantification of the Bubbling-, Turbulent- and Fast Fluidization- Flow Regimes and Void Structures.

Author names and Affiliations:

Jean Saayman[1]*, Willie Nicol[1], J. Ruud van Ommen[2] and Robert F. Mudde[2]

[1] *Department of Chemical Engineering*
University of Pretoria - Main Campus
Corner Lynwood Rd & Roper St
Hatfield
Pretoria
0002
South Africa

[2] Department of Chemical Engineering
Delft University of Technology
Julianalaan 136
2628 BL Delft
The Netherlands

* *Corresponding author:* **Jean Saayman**

Email: jeansaayman@gmail.com
Phone: +27 84 5134079
Postal Address: *Department of Chemical Engineering*
University of Pretoria - Main Campus
Corner Lynwood Rd & Roper St
Hatfield
Pretoria
0002

Abstract

Multiple fluidization regimes were studied using X-ray tomography. Geldart B sand particles were used in a 14cm (ID) column with a dual cyclone return system. Cross sectional solids concentration (ϕ) was measured and the time averaged ϕ ($\bar{\phi}$) decreased with velocity and axial height except in the turbulent regime where $\bar{\phi}$ remained constant. Radial profiles of $\bar{\phi}$ decreased to the centre, while all turbulent regime velocities resulted in similar radial $\bar{\phi}$ profiles. Results confirm the bubbling-turbulent transition velocity (U_c) determined from pressure fluctuations is a reliable quantification technique. The system exhibited slugging behaviour at higher bubbling regime velocities with voids taking on cylindrical shapes. Turbulent regime voids were characterized by elongated cylinders with diameters slightly less than the bubbling regime's slugs or fast fluidization regime's core annulus. Distribution curves of the ϕ signal indicated a distinct dense phase in the bubbling and turbulent regime with a velocity independent solid concentration. Void velocity analysis suggested that the bubble linking algorithm was unable to detect fast rising voids at higher velocities.

KEYWORDS: Fast X-Ray Tomography; Void Behaviour; Cross-Sectional Solids Concentration; Fluidization Flow Regime Characterization

1. Introduction

Gas-solid fluidized beds have complex hydrodynamics and solid distributions. Understanding these parameters' fundamental behaviour is important to gain insight in gas-solid contacting and in turn, reactor performance. Different intrusive and non-intrusive techniques have been used to measure solids distributions and void structures; some of these techniques include optical probes, Laser Doppler Anemometry (LDA), cross-sectional wire mess sensors, Electrical Capacitance Tomography (ETC), X-Ray Densitometry/Tomography, Gamma-Ray Densitometry and Nuclear Particle Tracking (CARPT and PEPT) [1]. Refer to [1] for an extensive review on the advantages/disadvantages of these techniques. X-Ray Tomography (XRT) is a useful, non-intrusive technique. At present 2D radiographic projections [2], single beam Ultrafast XRT [3] and multiple beams Fast XRT [4] are being used. The hydrodynamics of the bubbling and fast fluidization regimes are rather well understood, but interest in the turbulent regime has only strongly increased in the last two decades. Proper understanding of the flow structures in turbulent beds is still in its infancy with the initial investigations employing optical probes and Electrical Capacitance Tomography (ECT) techniques [5–8].

ECT has been widely applied in recent years. A very comprehensive ECT study is that of Makkawi and Wright, which spanned several regimes for a shallow bed [8,9]. Glass ballotini particles (Geldart B) were used for the bubbling, turbulent and fast fluidization regime and the aim was to define fluidization regimes based on these measurements. The investigation was limited to a shallow bed and axial measurements where not possible. Du et al. [10] used Electrical Capacitance Tomography (ECT) in conjunction with an optical probe to investigate bed non-homogeneity using Fluid Catalytic Cracking (FCC) catalyst for the bubbling and turbulent regime. The radial solids concentration profile

for this Geldart A particle system was found to be asymmetrical for the bubbling regime, but symmetrical for turbulent. The observation was made that ECT and the optical probe yield considerably different results for the void phase fraction depending on the threshold level distinguishing between the emulsion phase and the void phase. Ellis et al. [6] used optical fibre probes with FCC in columns with different diameters. The bubbling and turbulent regime was investigated. Asymmetry was found at the solids return inlet and bed surface, however, radial symmetry was observed for the rest of the bed. They reported some uncertainty due to the intrusive nature of the probes. Zhu et al. [7] installed three optical probes around the periphery of a fluidized bed at the same radial position. Similar to Ellis et. al. [6], Geldart A FCC catalyst was used in the bubbling and turbulent regime. No radial symmetry for the solids concentration profile was observed in the bubbling regime whereas symmetry did exist in the turbulent regime.
ECT is a fairly inexpensive method of tomography, but the resolution to the centre of the bed is relatively poor [11]. This disadvantage is due to the fact that ECT is a soft-field technique, which means the gas-solids distribution influences the position of the field lines. Fast X-Ray Tomography (XRT) does not suffer this disadvantage. XRT is a hard field technique: the direction of a field line is not changed by the medium. Rautenbach et al. [12] report a comparative study between ECT and XRT. Recent advances in fast XRT makes it possible to implement time-resolved cross-sectional measuring in fluidized beds [1]. The fast XRT technique has proven useful for visualization of bubbles at low operating velocities, and in previous work it was shown that reliable cross-sectional solids concentration measurements can be obtained using fast XRT [4,11,13,14].
These advances create the opportunity for new insights in bubble behaviour and cross sectional solids distribution. XRT has been proven for lower velocities [4,11,13,14] but not yet at the faster velocities of the turbulent and fast fluidization regimes where different solid distributions are expected. The quality of tomographic reconstruction and void visualisations in these regimes require exploration. The aim of this paper is to gain additional insight on the structure of the bed, with focus on the turbulent regime. The solids concentration profiles are determined and will be compared to literature. The flow structures of the bubbling-, turbulent- and fast fluidization regimes will be observed and the validity of two-phase theory is investigated.

2. Experimental

This investigation was conducted in an acrylic column 0.14 m in diameter and 1.4 m high. Two absolute-pressure sensors are installed, one in the plenum chamber and one 0.07 m above the distributor. Positioned around the column are 3 X-ray sources. Opposite to each X-ray source is a detector array; each array has a top and bottom row of 32 detectors, creating 64 lines of measurement through the column per source. This arrangement also results in two measuring planes separated by approximately 10.9 mm. All 192 detectors records at a rate of 2500Hz. The basic setup is the same as the one used by Mudde [4], with the exception of a smaller column and source circle diameter [1,13]. For more details on X-ray physics, please refer to these articles. Figure 1 illustrates the setup as viewed from the top and side view. At a specific superficial velocity and measuring height signals were logged for 300 seconds; Makkawi and Wright [5] recommend at least 120 seconds.
The column is filled with sand, having a Sauter mean diameter of 101 μm and a solids density of 2530 kg/m^3, to a static bed height of 0.50 m. Air at ambient temperature and pressures is used as

fluidizing medium and the achievable velocity range of the setup is 0.11 m/s up to 2.6 m/s. Four measuring heights above the distributor were investigated: 0.20m, 0.30m, 0.40m and 0.50m.

INSERT FIGURE 1

Figure 2 illustrates the first 16 measuring lines of a single source. The attenuation on each line is compared to that of packed bed and translated into line solid fraction. (ϕ_i). A calibration was performed for each individual detector. Calibration points are obtained by placing a thin acrylic partition in the column at different positions and filling one side with material. Partition positions are indicated by the horizontal lines in Figure 2. Using the following calibration function, A_{cal}, B_{cal} and C_{cal} can be determined for each individual detector:

$$I_{Xray} = A_{cal} + B_{cal} \exp\left({}^{-x}/_{C_{cal}}\right) \quad (1)$$

where, $I_{X\text{-}ray}$ is the beam intensity and x is the amount of material between the source and detector. A weighted average between all 32 lines is calculated to obtain a cross-sectional solids fraction (ϕ). The weighting factor is based on each detector's line length (l_i) penetrating the bed. An average is taken between the values obtained from each detector-source pair:

$$\phi = \frac{1}{3}\left\{\left(\sum_{i=1}^{32}\frac{l_i}{l_T}\phi_i\right)_{source1} + \left(\sum_{i=1}^{32}\frac{l_i}{l_T}\phi_i\right)_{source2} + \left(\sum_{i=1}^{32}\frac{l_i}{l_T}\phi_i\right)_{source3}\right\} \quad (2)$$

where:

$$l_T = \sum_{i=1}^{32} l_i \quad (3)$$

For these calculation 5 minutes of data was processed for both top and bottom measurement planes. Figure 3a illustrates the resulting cross-sectional solids concentration measurement. Movement of a void (or void agglomerates) through the planes is associated with a drastic drop in solids concentration. A time lag of voids crossing the detection planes is clearly observed in Figure 3.

INSERT FIGURE 2

An average void rise velocity (U_v) can be determined using the signals of both bottom and top planes. A similar method to the bubble linking algorithm of Rüdisüli et al. [15] is used. The Sum of Squared Differences (SSD) between the bottom and top plane can be calculated using both 5 minute signals. The whole top plane signal is then shifted in time until a minimum in the SSD is obtained. Figure 3 illustrates this technique: (a) is the original signals, (b) and (c) are the same signals, with the exception of the top plane signal being shifted in time. (d) shows the SSD as the top plane signal is shifted. **a**, **b** and **c** indicate the SSD of Figures 3a, 3b and 3c. The best agreement between the bottom and top signal is achieved at point **b.** At this time shift the SSD is at a minimum. This time shift value can be interpreted as the averaged time voids take to move from the bottom plane to the top plane. By knowing the distance between the two planes a velocity can be calculated (U_v). Each bubble will have its own rise velocity depending on its size; U_v is however the time-averaged void rise velocity.

INSERT FIGURE 3

3. Results and Discussion

3.1 Regime quantification

The standard deviation of pressure fluctuation at the different velocities is shown in Figure 4. The measurements were repeated three times and the average was calculated for each velocity. The bubbling to turbulent transition (U_c) is defined as the velocity at which the standard deviation reaches a maximum. This is the point where the amplitude of the pressure fluctuation is at its largest. Using this method, U_c was determined to be 0.65 m/s. Table 1 reports the top 4 Geldart B U_c-correlations, in order of preference as recommended by Arnaldos and Casal [16]. Also reported are their individual predictions for this specific system. Proper agreement is obtained for the two highly recommended correlations.

The coherence between the pressure measurement signal in the plenum chamber and in the bed is calculated [17]. The standard deviation of the incoherent part of the pressure signal is a measure of void sizes. It can be seen that the voids grow as the superficial velocity is increased in the bubbling regime and reach a maximum stable size in the turbulent regime. The sudden variation in the data and increase in the averages beyond 1.19 m/s is due to the core-annulus structure which forms in the centre of the reactor; this is considered to be the start of the fast fluidization regime and is indicated on Figure 4 as U_k. The use of U_k is not undisputed [18], however for this case it agrees reasonably well with the sudden increase in the standard deviation of the incoherence. The value of U_k is determined to be 1.19 m/s.

INSERT FIGURE 4

INSERT TABLE 1

3.2 Mean solids concentration

Figure 5 shows the 5 minute time averaged mean of the cross-sectional solids fraction ($\overline{\phi}$) obtained from the X-ray data for the bottom plane. Makkawi and Wright found a 20 second measurement to be quite sufficient [9]. Three distinct types of behaviour are observed which coincide with the different regimes. A sharp decrease in $\overline{\phi}$ with velocity can be seen in the bubbling regime with a more rapid decrease observed higher up in the reactor. Zhu et al. [7] observed similar height dependence using optical probes. The gradient of $\overline{\phi}$ changes for the turbulent regime; the same trend was seen by Makkawi and Wright [8] using ECT from the single height measurement. The solids concentrations levels off and remains fairly constant with velocity at H = 400 mm and H = 500 mm. At the highest gas velocity in the turbulent fluidization regime, $\overline{\phi}$ at 200 mm, 300 mm and 400 mm are the same, while it is lower at 500 mm. The packed bed height was 500 mm; therefore this measurement is close to the splash zone. The decreasing trend continues in the fast fluidization regime. In the fast fluidization regime there is no difference with height, except for measurements at

500 mm, which is at the dense bed surface where one would expect lower $\overline{\phi}$. Pneumatic transport is observed to sets in at 2.60 m/s. There is a good correlation between the observed solids fraction behaviour as the different flow regimes set in and the traditional pressure based regime quantification techniques. The tomographic results confirm the determination of U_c from pressure signals.

INSERT FIGURE 5

The fan geometry of the measurement lines and the fact that the measurement lines penetrate the column from one side to the other; prevented the acquisition of true radial profiles. However, to get an impression of the radial solids distribution the mean line solids fractions ($\overline{\phi_i}$) of each detector for a single source is indicated in Figure 6. Only 2 minutes of data were used to calculate the mean of each line. The values of the outer most detectors are not shown. Due to the close proximity of the detection line to the wall, column vibrations influenced the outer detector value. Between 0.55m/s and 0.83m/s radial profiles are fairly constant, which suggests, as with $\overline{\phi}$, the radial solids distribution remains constant as well. At the lowest superficial velocity asymmetry is observed, the asymmetry is due to low distributor pressure drop causing mal-distribution. At high velocities pressure drop across the distributor increases and better symmetry is observed. Slight deviation from symmetry is likely caused by the solids return inlet coming from the cyclone system. Ellis et al. noted a similar effect due to the solids return [6].
At 200 mm smooth profile contours are obtained for all velocities. Axially higher up in the column a spike in the radial centre is seen, which disappears as the Fast Fluidization regime is reached. This cannot be attributed to mal-distribution since it is not observed at 200 mm. The bubble wake geometry can provide a plausible explanation, where the high solid density wake of the bubble appears frequently in the centre of the column, with a leaner ring structure surrounding the wake. Using tomographic reconstructions, discussed in section 3.4, the wake-ring structure could be observed. This would explain the centre spike in solid density, which will disappear when the core-annulus structure of fast fluidization is formed. Bubbles were undeveloped lower down in the column which is why it is not seen at 200 mm, higher up bubbles merged and grew, moving up in the centre of the column.

INSERT FIGURE 6

3.3 Solids concentration distributions

Figure 7 shows the density distributions of the ϕ signals at different velocities and heights. The distributions are based on 5 minutes of data. Unimodal and bimodal curves are observed. The bimodal curves indicate that two distinct phases exist. The peak at higher solid concentration would represent the dense phase, whereas the lower peak would represent the lean phase (bubbles and voids). The lean phase peak is less defined due to the simultaneous presence of voids and emulsion over the cross section; for a dense phase peak voids can be completely absent. In the case of a unimodal trend the signal does not fluctuate between the two phase. The conclusion can be drawn that the structure which exist in the bed remains fairly constant with time. The trend at 200 mm is considerably different from the trends higher up in the column, especially for the turbulent regime.

The distributions at 200 mm tend to be unimodal. It is unlikely that a core annulus exists at the low velocity. In this case the trend can be explained by single or multiple small bubbles passing frequently through the cross sectional measurement plane, causing shorter periods of complete cross sectional dense phase to be recorded; all the time a spatial average of bubbles and dense phase is recorded.
The bubble regime has a clear bimodal trend, with large dense phase peaks. Since it is know that the fast fluidization regime is characterized with a constant core annulus structure a unimodal trend is expected and noted in the results. For the turbulent regime the mean cross sectional solids concentration and radial solids concentration profiles (Figure 5 and 6) shows constant values with velocity. However, the density distributions differ slightly with regards to velocity. The fact that dense phase peaks exist in the turbulent regime is also noteworthy. This observation indicates that times exist when the cross section (higher up in the column) contains no voids. It should also be noted that the median of the dense phase peak does not change significantly with velocity.

INSERT FIGURE 7

3.4 Void rise velocity and tomographic reconstructions

Figure 8 shows the result of the calculated average void rise velocity (U_v). U_v increases significantly in the bubbling regime with superficial velocity. As the superficial velocity is increased into the turbulent regime U_v is still increasing, however for the bottom part of the column (at 200 mm), voids reach a constant velocity fairly quickly. This trend agrees well with the observed trend in the standard deviation of incoherence of Figure 2. The pressure probe was also in the bottom section of the column. Measurements higher up in the column all fall in a band where U_v levels off but does not necessarily reach a constant value. It seems even though cross sectional solids concentrations become independent of the superficial velocity in the turbulent regime, void dynamics does not. U_v in the fast fluidization regime has no clear trend and seemed to be random. These random values occur since there are no more distinct voids rising; rather a core-annulus structure forms, which fluctuates causing random minimums in the SSD's.

INSERT FIGURE 8

The data from the two measurement planes were processed using a Simultaneous Algebraic Reconstruction Technique (SART). This technique is an iterative reconstruction algorithm by which an instantaneous cross sectional image of the bed is obtained. For more details on the reconstruction algorithm see previously published work on the technique [4,11,13]. Figure 9 is an example of such a reconstructed image for both the bottom and top plane at the same point in time. A cross section of the bubble nose is seen in the top plane, where as a cross section of the same bubble lower down is seen in the bottom plane.
Signal noise, inherent to the X-Ray sensors, was eliminated by averaging over 10 samples. 55 by 55 pixel images were reconstructed, resulting in a 2.54mm pixel length. Pixels outside the column diameter where automatically assigned a zero value. Given the 2500Hz acquisition frequency, reconstruction resulted in 250 images per second. The images were stacked for both the top and bottom plane and a pseudo 3D representation of bubbles/voids could be obtained. The z-axis has time as scale and therefore the true length dimension of the bubble is not given. Figure 10 shows

the results of this entire process for 2 seconds of data, 300 mm above the distributor and a superficial velocity of 0.11 m/s.

INSERT FIGURE 9

INSERT FIGURE 10

Figure 11 shows samples of the bottom and top plane reconstructions for the bubbling regime (U_0 = 0.43m/s) and turbulent regime (U_0 = 0.87m/s) at 2 different heights (H = 200mm and H = 400mm). Using the calculated average void rise velocity (U_v) the z-axis was converted from a time to length time scale. Very good agreement is seen between the two planes. Slugs were observed during experimental runs and the plug like slugs are clearly visible at U_0 = 0.43m/s, H = 400mm. For the turbulent regime slug-like structures are seen, however visually these voids look to have smaller cross sections than slugs. The turbulent regime's flow structures are more closely represented by a train of highly elongated bubbles. This could be the start of a core annulus which collapse momentarily.

INSERT FIGURE 11

The technique of Brouwer et. al. [19] was used to determine volume equivalent bubble diameters. To do this, the individual rise velocity of each bubble is required. Using the pseudo 3D images and an object matching algorithm, bubbles are identified and matched between the bottom and top plane reconstructions. This matching is done on the basis of similar position in the x-y plane, similar volume of the pseudo 3D bubble and a maximum allowable bubble rise velocity. Once bubbles are matched; the time it takes for a bubble's centroid to rise from the bottom plane to top plane is determined. Using this time and the fact that the planes are 10.9 mm apart, it is possible to determine the rise velocity and thereby the true volume of the bubble. Three parameters for every void passing the measurement plane can be determined:

- Void volume - V_b
- Void length (Distance from bubble nose to wake) - L_b
- Void velocity - $U_{b\text{-}Tomo}$

Due to the computational intensiveness of the analysis procedure the shortest significant signal lengths were employed. Initial signal periods of 2.5 s were taken and doubled until the mean bubble volume (V_b) changed with less than 5%. A minimum of 10 seconds of data was required before d_b remained unchanged for the low velocity measurements. Table 2 shows the signal length required for each experiment's analysis and the number of objects that could be matched. The bubbling and turbulent regimes are analysed, the fast fluidization regime is characterized with a core annulus structure which cannot be quantified in this manner. Figure 12 shows the percentage of objects that could be matched. More than 50 % of voids could be matched in the bubbling regime, but the turbulent regime is more erratic leading to lower fractions of matching. Since it is unclear whether this is partly due to limitations of the XRT reconstruction or matching algorithm, care should be taken not to draw quantitative conclusions.

INSERT TABLE 2

INSERT FIGURE 12

3.5 Reconstruction analysis

This final discussion will be based on overall bed averages, the average values between the different measuring heights. From the discussion thus far it is evident hydrodynamic behaviour is not fully developed at 200 mm. The data from this measurement height will therefore be excluded from the averages. Figure 13 shows the measured void parameters: Void volume (a), void length (b) and the cylindrical diameter (c) if the assumption is made voids are cylinder shapes, Figure 13 (d) confirms this assumption is a reasonable one, the figure shows the void volume is directly proportional to void length. Theory suggests that U_c is the point at which the largest stable bubbles exist, after U_c bubbles breakup in smaller transient voids [20]. A decrease in void volume, as well as length is seen to occur at U_c, after which both continue to increase. However, the cylindrical diameter continues to decrease, confirming that the structures are thinner elongated bubbles. In the Zhang and Bi optical probe study of void behaviour [21] it was found that void lengths decrease in the turbulent regime. Their investigation was however performed on Geldart A particles while the optical probe is a local measurement which has a higher and more defined spatial resolution.

INSERT FIGURE 13

Two seconds of reconstructed fast fluidization regime pseudo-3D images are shown in Figure 14 (U_0 = 1.84 m/s). Since the core annulus is a continuous structure the z-axis cannot be scaled using a velocity as was done for Figure 11. It was found from these reconstructions that the diameter of the core annulus increases with height and is in the range of 9 cm to 11 cm. Similar reconstructions were done for data at U_0 = 1.19 m/s and it was confirmed the core annulus structure started forming at 1.19 m/s.

INSERT FIGURE 14

The expanded bed height in the turbulent regime is approximately 1 m and the void lengths are 0.4 m to 0.5 m, with cross sectional diameters of approximately 8 cm. Even though the turbulent regime has unique hydrodynamic behaviour, the structure of the voids seems to be a transient state between the bubbling- and fast fluidization- regime's flow structures. The structure in the turbulent regime is best described as an unstable core annulus or as thin elongated bubbles. This structure is most likely caused by the column diameter limitation and might not apply in larger diameter columns.

There are 3 methods to determine the void rise velocity. Two of which have been discussed, U_v and $U_{b\text{-}Tomo}$. The third method is a theoretical calculation based on a phase flow balance and the assumption that the emulsion phase flow is at minimum fluidization (U_{mf}), then the theoretical bubble rise velocity ($U_{b\text{-}Theo}$) is [22]:

$$\psi_B = \frac{U_0 - U_{mf}}{U_{b-Theo} - U_{mf}} \approx \frac{U_0}{U_{b-Theo}} \qquad (4)$$

$$U_{b-Theo} = \frac{U_0}{\psi_B} \quad (5)$$

Where the bubble phase fraction (ψ_B) is calculated using the cross sectional solids concentration:

$$\psi_B = \frac{\phi_s - \bar{\phi}}{\phi_s} \quad (6)$$

Figure 15 shows how the average rise velocity changes with the superficial velocity. Also indicated is the standard deviation of $U_{b\text{-}Tomo}$. Trend wise U_v and $U_{b\text{-}Theo}$ agree well although the absolute values are different. This difference is likely due to tolerance variation in the measurement of the distance between the two planes. $U_{b\text{-}Tomo}$ has a large standard deviation at higher superficial velocities. $U_{b\text{-}Tomo}$ is based on individual bubble measurements and such deviations are to be expected. An important observation is that the average $U_{b\text{-}Tomo}$ is much lower than U_v. As shown by Figure 12 a large number of detected objects could not be matched in both planes. From Figure 15 it would seem that the algorithm fails to match the relatively fast voids. The detection boundary for $U_{b\text{-}Tomo}$ is limited by the temporal resolution of the setup. With an approximate plane distance of 10.9 mm and a sampling rate of 250 Hz, the maximum detectable void rise velocity is 2.725 m/s. It is not clear from the graph, but it needs to be kept in mind the standard deviation only includes 68% of the data. The total distribution of data is cut off at 2.7 m/s Quantitative measurements relying on this algorithm should not be used for the turbulent regime. U_v is recommended as a more reliable measurement.

INSERT FIGURE 15

4. Conclusion

It was successfully shown that fast X-ray tomography can effectively measure cross sectional solids concentrations (ϕ) and be used for tomographic reconstruction at low and high superficial velocities. Distinct behaviour was observed for all the fluidization regimes. Determination and characterization of the regimes could be done using pressure measurements, solids fraction measurements and reconstructed tomography images. There was a good correlation between the observed solids fraction behaviour of the different flow regimes and the traditional pressure based methods of regime quantification. Tomographic results confirm U_c determined from pressure fluctuations is a reliable quantification technique for the bubbling-turbulent transition velocity.
Time averaged ϕ ($\bar{\phi}$) decreased with velocity and axial height, except in the turbulent regime where $\bar{\phi}$ remained constant. Radial profiles of $\bar{\phi}$ decreased to the centre of the bed while remaining similar for all velocities of the turbulent regime. Distributions of the ϕ signal showed a distinct dense phase present in the turbulent regime of which the solids concentration was independent of velocity.
The system exhibited slugging behaviour and with the aid of tomographic reconstructions it was shown that the voids can be characterized as cylindrical shapes. The turbulent regime voids were also cylindrical in shape with diameters less than the bubbling regime slugs or the fast fluidization regime core annulus. It was shown the turbulent regime has unique hydrodynamic behaviour although voids seem to be a transient structure between the bubbling- and fast fluidization-regime's void structures.

Three methods were used to determine void rise velocities. The first was a technique based on time-shift minimization between the top and bottom measurement plane; the second was based on theoretical equations and the third on individual rising voids. From these three velocity analyses it was concluded the bubble linking algorithm was unable to link fast rising voids.

Nomenclature

Ar	Archimedes number ($d_p^3.\rho_g.(\rho_s-\rho_g).g/\mu^2$)
A_{cal}	Calibration coefficient 1
B_{cal}	Calibration coefficient 2
C_{cal}	Calibration coefficient 3
d_b	Volume equivalent spherical bubble diameter(m)
$d_{b\text{-}Cyl}$	Cylindrical equivalent base diameter (m)
d_p	Particle diameter (m)
D_t	Column Diameter (m)
g	Gravitational constant (m/s^2)
H	Height above distributor (mm)
i	X-ray beam number (-)
L_b	Axial void length (m)
$I_{X\text{-}ray}$	X-ray beam intensity (au.)
I_i	Length of a single X-ray beam (i) inside the column (m)
I_T	Total length of X-ray beams in the column from a single source(m)
Re	Reynolds number ($d_p.u_o.\rho_g/\mu$)
$U_{b\text{-}Theo}$	Theoretical void rise velocity (m/s)
$U_{b\text{-}Tomo}$	Void rise velocity determined form individual bubbles rising (m/s)
U_0	Operating superficial velocity (m/s)
U_c	Turbulent transition velocity (m/s)
U_k	End of turbulent regime (m/s)
U_{mf}	Minimum fluidization velocity (m/s)
U_v	Average void rise velocity (m/s)
V_b	Void volume (m^3)
x	Amount of material on between X-ray source and detector (m)

Greek letters

ρ_g	Gas density (kg/m^3)
ρ_s	Solids density (kg/m^3)
μ	Viscosity (Pa.s)
ϕ	Instantaneous cross sectional solids fraction (-)
$\overline{\phi}$	Mean (time averaged) cross sectional solids fraction (-)
ϕ_e	Emulsion phase's solids fraction (-)
ϕ_i	Instantaneous line solids fraction (-)
$\overline{\phi_i}$	Mean (time averaged) line solids fraction (-)
Ψ_B	Lean/bubble phase fraction (-)

References

[1] R.F. Mudde, Advanced measurement techniques for GLS reactors, The Canadian Journal of Chemical Engineering. 88 (2010) 638–647.

[2] T.J. Heindel, J.N. Gray, T.C. Jensen, An X-ray system for visualizing fluid flows, Flow Measurement and Instrumentation. 19 (2008) 67–78.

[3] M. Bieberle, F. Barthel, U. Hampel, Ultrafast X-ray computed tomography for the analysis of gas–solid fluidized beds, Chemical Engineering Journal. 189-190 (2012) 356–363.

[4] R.F. Mudde, Bubbles in a Fluidized Bed : A Fast X-Ray Scanner, AIChE Journal. 57 (2011) 2684–2690.

[5] B. Du, L. Fan, F. Wei, W. Warsito, Gas and Solids Mixing in a Turbulent Fluidized Bed, AIChE Journal. 48 (2002) 1896–1909.

[6] N. Ellis, H.T. Bi, C.J. Lim, J.R. Grace, Hydrodynamics of turbulent fluidized beds of different diameters, Powder Technology. 141 (2004) 124–136.

[7] H. Zhu, J. Zhu, G. Li, F. Li, Detailed measurements of flow structure inside a dense gas–solids fluidized bed, Powder Technology. 180 (2008) 339–349.

[8] Y.T. Makkawi, P.C. Wright, Fluidization regimes in a conventional fluidized bed characterized by means of electrical capacitance tomography, Chemical Engineering Science. 57 (2002) 2411–2437.

[9] Y.T. Makkawi, P.C. Wright, Electrical capacitance tomography for conventional fluidized bed measurements—remarks on the measuring technique, Powder Technology. 148 (2004) 142–157.

[10] B. Du, W. Warsito, L. Fan, Bed Nonhomogeneity in Turbulent Gas-Solid Fluidization, AIChE Journal. 49 (2003) 1110–1126.

[11] R.F. Mudde, Time-resolved X-ray tomography of a fluidized bed, Powder Technology. 199 (2010) 55–59.

[12] C. Rautenbach, R.F. Mudde, X. Yang, M.C. Melaaen, B.M. Halvorsen, A comparative study between electrical capacitance tomography and time-resolved X-raytomography, Flow Measurement and Instrumentation. 30 (2013) 34–44.

[13] R.F. Mudde, Double X-ray Tomography of a Bubbling Fluidized Bed, Industrial & Engineering Chemistry Research. 49 (2010) 5061–5065.

[14] M. Wormsbecker, T. Pugsley, J.R. Van Ommen, J. Nijenhuis, R. Mudde, Effect of Distributor Design on the Bottom Zone Hydrodynamics in a Fluidized Bed Dryer Using 1-D X-ray Densitometry Imaging, Industrial & Engineering Chemistry Research. 48 (2009) 7004–7015.

[15] M. Rudisuli, T.J. Schildhauer, S.M. Biollaz, J.R. Van Ommen, Bubble characterization in a fluidized bed by means of optical probes, International Journal of Multiphase Flow. 41 (2012) 56–67.

[16] J. Arnaldos, J. Casal, Prediction of transition velocities and hydrodynamical regimes in fluidized beds, Powder Technology. 86 (1996) 285–298.

[17] J. Van der Schaaf, J.C. Schouten, F. Johnsson, C.M. Van den Bleek, Non-intrusive determination of bubble and slug length scales in fluidized beds by decomposition of the power spectral density of pressure time series, International Journal of Multiphase Flow. 28 (2002) 865–880.

[18] H.T. Bi, N. Ellis, I.A. Abba, J.R. Grace, A state-of-the-art review of gas-solid turbulent fluidization, Chemical Engineering Science. 55 (2000) 4789–4825.

[19] G.C. Brouwer, E.C. Wagner, J.R. van Ommen, R.F. Mudde, Effects of pressure and fines content on bubble diameter in a fluidized bed studied using fast X-ray tomography, Chemical Engineering Journal. 207-208 (2012) 711–717.

[20] K. Dubrawski, S. Tebianian, H.T. Bi, J. Chaouki, N. Ellis, R. Gerspacher, et al., Traveling column for comparison of invasive and non-invasive fluidization voidage measurement techniques, Powder Technology. 235 (2013) 203–220.

[21] X. Zhang, H.T. Bi, Study on Void Behavior in a Turbulent Fluidized Bed with Catalyst Powders, Industrial & Engineering Chemistry Research. 49 (2010) 6862–6869.

[22] D. Kunii, O. Levenspiel, Fluidization Engineering, 2nd ed., Butterworth-Heinemann, 1991.

Captions

Figures:

Figure 1*: Top view of the fast XRT setup showing the 3 detector arrays and sources. Side view showing a single upper and lower detector array (based on from Mudde* [4]*).*

Figure 2*: Position of 16 measuring lines (half of a single detector array). Horizontal lines indicate positions of the partitions used for calibration.*

Figure 3*: (a) is an example of the calculated cross sectional solids concentration signal obtained for both top and bottom measuring planes. The example is taken from the measurement done at 200mm above the distributor and at a velocity of 0.11 m/s. (b) and (c) shows the same signal, except the top plane's signal is shifted in time. (d) is the calculated SSD between the top and bottom plane signals at different top plane time shifts.*

Figure 4*: Standard deviation of pressure fluctuations, showing the bubbling to turbulent regime transition (U_c) at 0.65 m/s. Also shown is the standard deviation of incoherence, which is a measure of the void size. The end of turbulent fluidisation (U_k) is determined to be 1.19 m/s.*

Figure 5*: The average cross sectional solids concentration with superficial velocity at H=200mm, H=300mm, H=400mm and H=500mm from the distributor.*

Figure 6*: Mean line solid fraction indicating radial distribution of solids. Bold markers indicate U_c and U_k. Regime indication given in velocity legend.*

Figure 7*: The density distributions of the cross sectional solids concentration (Φ) at different heights. The y-axis is normalized to ensure the area under each distribution curve is unity.*

Figure 8*: Average void movement. Data beyond 1.8 m/s are not shown since values are random in the fast fluidization regime. These random values occur due to the absence of distinct rising voids.*

Figure 9*: Reconstructed cross sectional image for the bottom and top plane. Both images are taken at the same point in time. This example is taken from the measurement at a height of 300 mm and a superficial velocity of 0.11 m/s.*

Figure 10*: Pseudo 3D reconstruction of the void shapes over 2 seconds. H = 300mm and U_0 = 0.11 m/s. The y- and x-axis give length dimensions while the z-axis is represented in time. t=0 s at top and t=2s at bottom.*

Figure 11*: Three samples of 2 second reconstructions for the bottom and top planes at two superficial velocities (Bubbling - U_0 = 0.43m/s and Turbulent - U_0 = 0.87m/s) and heights (H = 200mm and H = 400mm) are shown. "B" indicates bottom plane and "T" indicates top plane.*

***Figure 12**: Fraction of objects which could be matched in both bottom and top planes.*

***Figure 13**: Quantification of void structure. The average void volume (a), void length (b) of the 300 mm, 400 mm and 500 mm is shown. If the assumption is made the voids area cylindrical the cylindrical diameter (c) can be calculated. (d) confirms this assumption is a reasonable one, the void volume is directly proportional to void length.*

***Figure 14**: Illustration of the core annulus at different heights in the column. U_0 = 1.84m/s.*

***Figure 15**: Comparison of different methods for determining the average rise velocity of voids.*

Tables:

***Table 1**: U_c correlations and predictions of the system under investigation* [16].

***Table 2**: Signal lengths analysed to determine mean bubble diameter*

TABLE 1

Authors	Equation	Predicted value (m/s)
Jin et al. [16]	$U_c = (gd_p)^{0.5}[\frac{(KD_f)(\rho_s - \rho_g)}{d_p\rho_g}]^{0.27}$ $KD_f = 0.00367$ (for free bed)	0.66
Cai et al. [17]	$U_c = (gd_p)^{0.5}[\frac{0.211}{D_t^{0.27}} + \frac{2.42 \times 10^{-3}}{D_t^{1.27}}][\frac{D_t(\rho_s - \rho_g)}{d_p\rho_g}]^{0.27}$	0.68
Nakajima et al. [18]	$Re_c = 0.633Ar^{0.467}$	0.79
Lee and Kim [19]	$Re_c = 0.7Ar^{0.485}$	0.95

TABLE 2

Flow (m/s)	Signal length analysed in seconds (Number of voids detected are indicated)			
	200 mm	300 mm	400 mm	500 mm
0.11	10 (72)	10 (40)	10 (26)	10 (26)
0.22	10 (38)	10 (28)	20 (37)	20 (31)
0.32	20 (56)	20 (47)	20 (37)	20 (27)
0.43	20 (43)	20 (39)	20 (33)	20 (25)
0.54	20 (32)	20 (23)	20 (29)	20 (28)
0.65	20 (21)	40 (15)	40 (42)	40 (52)
0.76	40 (38)	40 (42)	40 (52)	40 (56)
0.87	40 (13)	40 (18)	40 (45)	40 (49)
0.97	40 (24)	40 (21)	40 (26)	40 (33)

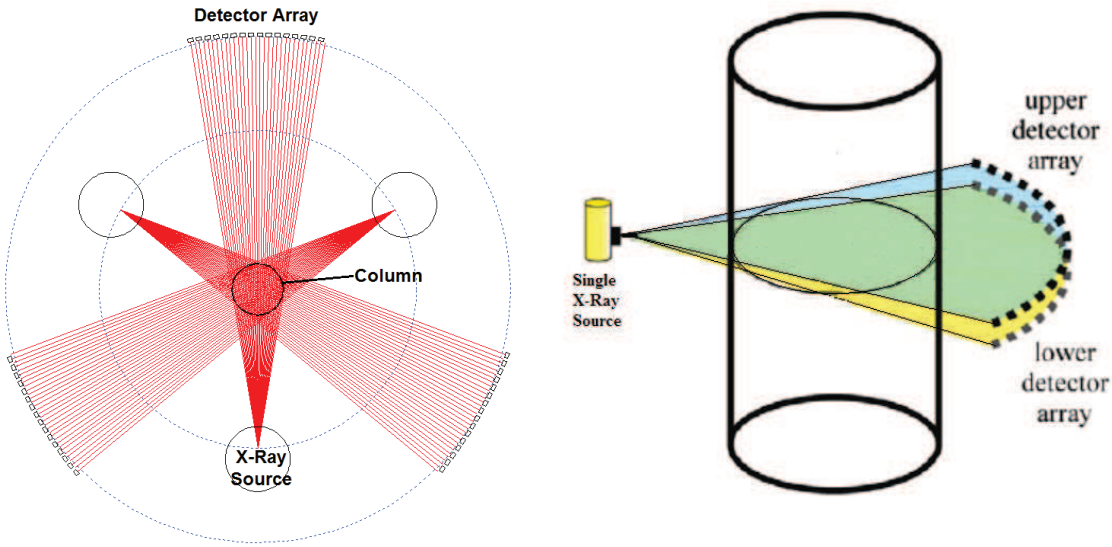
Detector Array
Column
X-Ray
Source
upper
detector
array
Single
X-Ray
Source
lower
detector
array

FIGURE 1

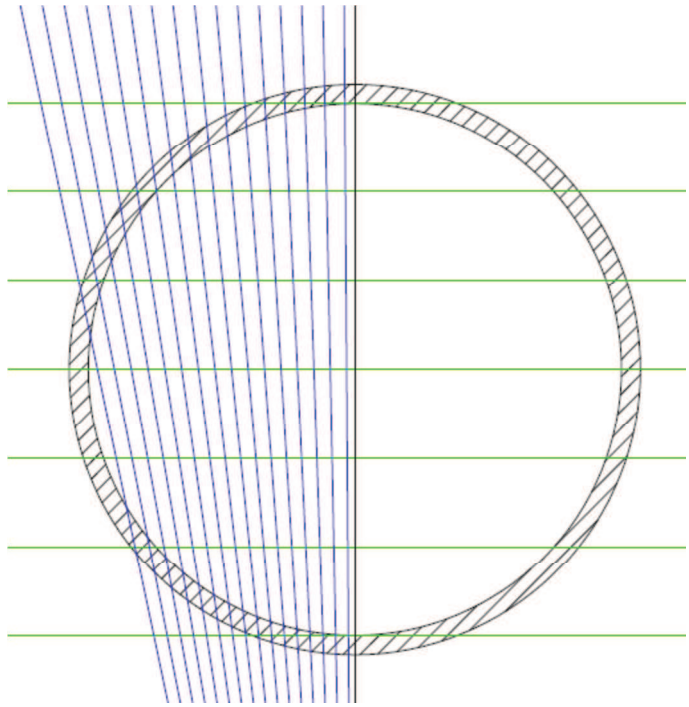

FIGURE 2

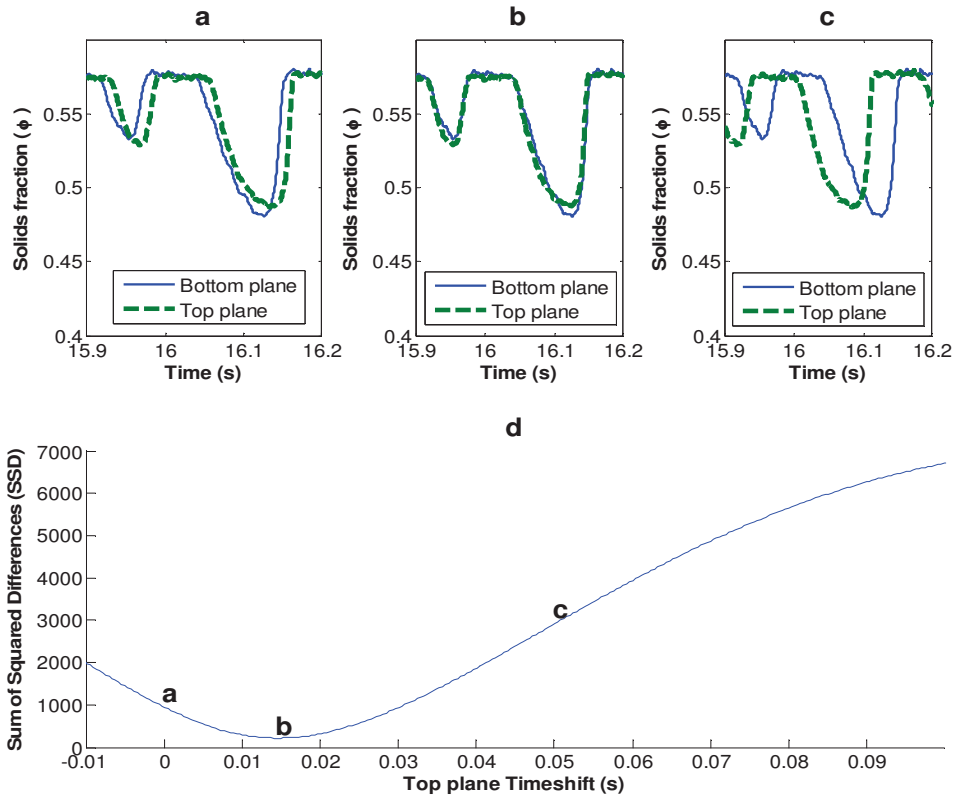
a
b
c
Solids fraction (ϕ)
0.55
0.5
0.45
0.4
15.9
16
16.1
16.2
Time (s)
Bottom plane
Top plane
d
Sum of Squared Differences (SSD)
7000
6000
5000
4000
3000
2000
1000
0
-0.01
0
0.01
0.02
0.03
0.04
0.05
0.06
0.07
0.08
0.09
Top plane Timeshift (s)

FIGURE 3

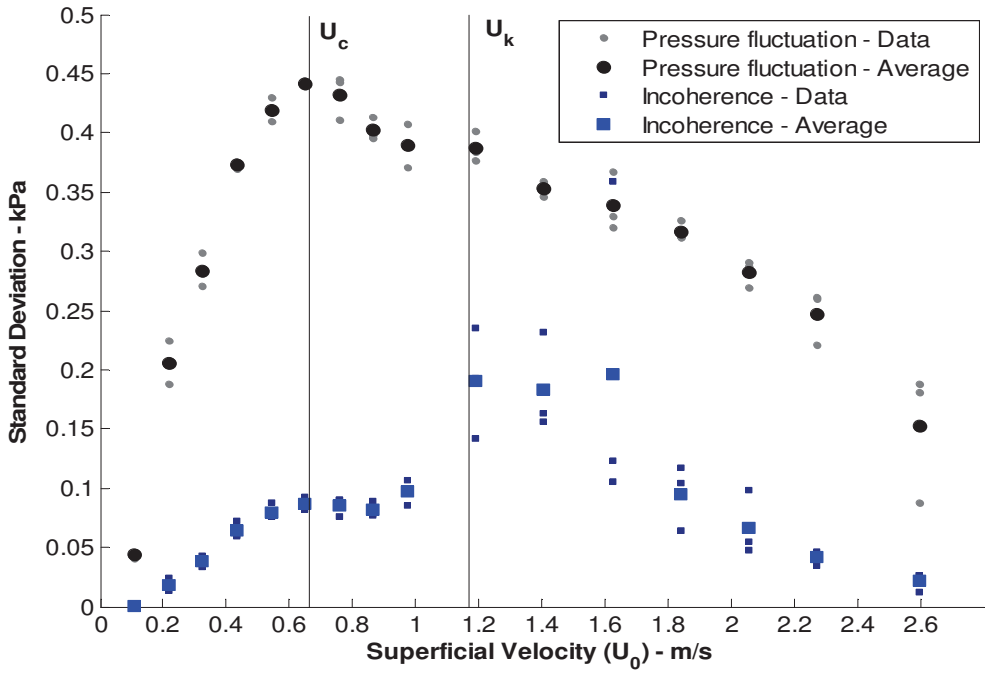
Standard Deviation - kPa
Superficial Velocity (U_0) - m/s
U_c
U_k
Pressure fluctuation - Data
Pressure fluctuation - Average
Incoherence - Data
Incoherence - Average
0
0.05
0.1
0.15
0.2
0.25
0.3
0.35
0.4
0.45
0.5
0.2
0.4
0.6
0.8
1
1.2
1.4
1.6
1.8
2
2.2
2.4
2.6

FIGURE 4

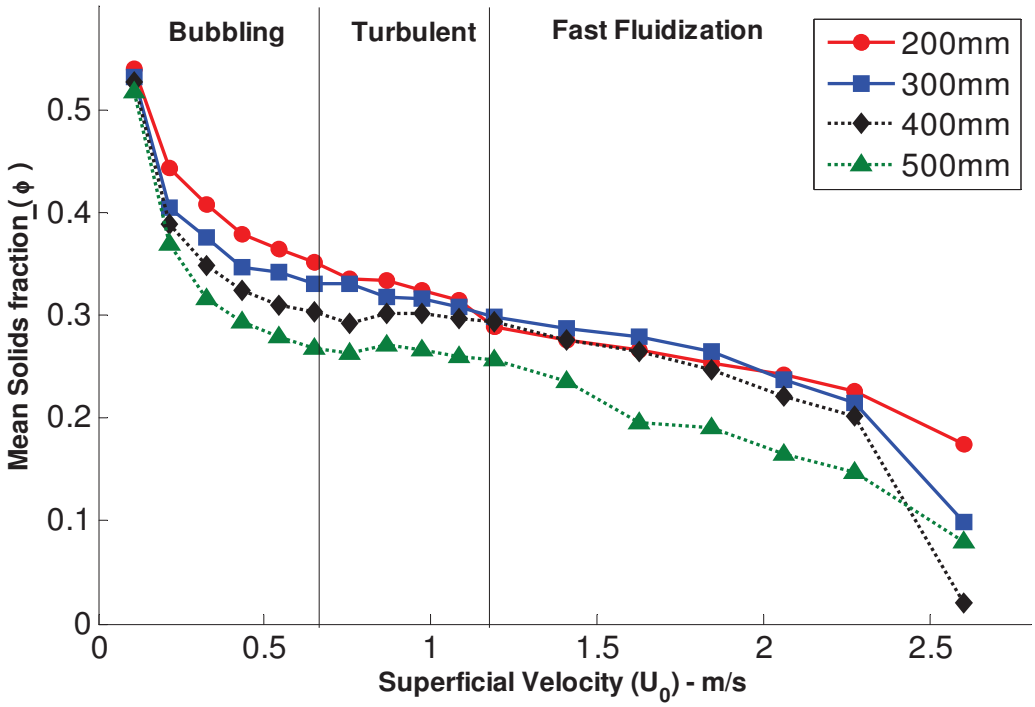
Bubbling
Turbulent
Fast Fluidization
200mm
300mm
400mm
500mm
Mean Solids fraction (ϕ)
0
0.1
0.2
0.3
0.4
0.5
0
0.5
1
1.5
2
2.5
Superficial Velocity (U0) - m/s

FIGURE 5

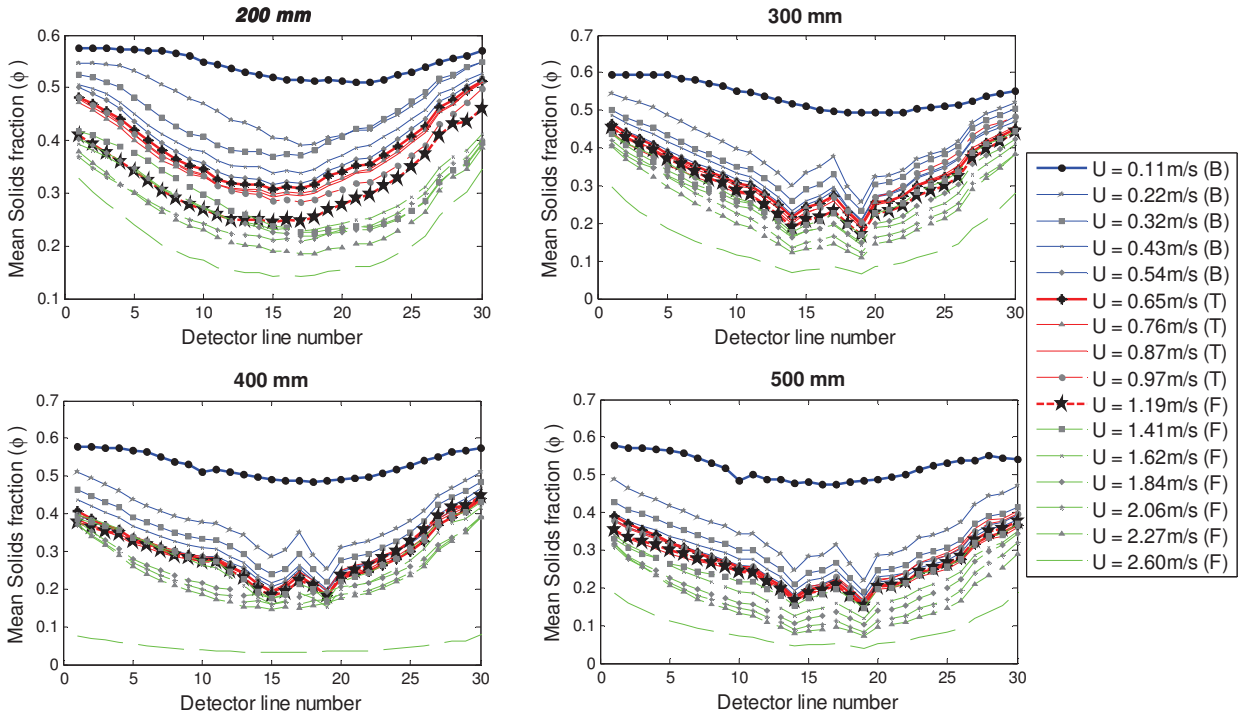
200 mm
300 mm
400 mm
500 mm
Mean Solids fraction (ϕ)
Detector line number
U = 0.11m/s (B)
U = 0.22m/s (B)
U = 0.32m/s (B)
U = 0.43m/s (B)
U = 0.54m/s (B)
U = 0.65m/s (T)
U = 0.76m/s (T)
U = 0.87m/s (T)
U = 0.97m/s (T)
U = 1.19m/s (F)
U = 1.41m/s (F)
U = 1.62m/s (F)
U = 1.84m/s (F)
U = 2.06m/s (F)
U = 2.27m/s (F)
U = 2.60m/s (F)

FIGURE 6

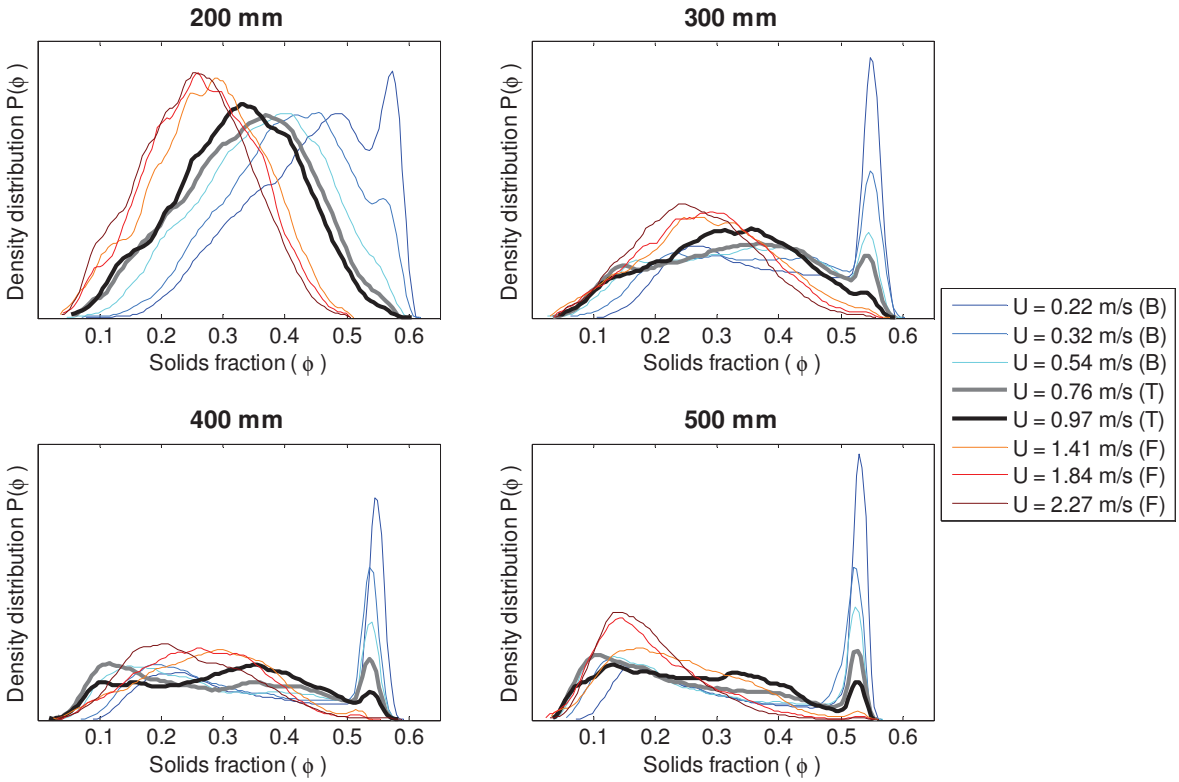
200 mm
300 mm
400 mm
500 mm
Density distribution P(ϕ)
Solids fraction (ϕ)
0.1
0.2
0.3
0.4
0.5
0.6
U = 0.22 m/s (B)
U = 0.32 m/s (B)
U = 0.54 m/s (B)
U = 0.76 m/s (T)
U = 0.97 m/s (T)
U = 1.41 m/s (F)
U = 1.84 m/s (F)
U = 2.27 m/s (F)

FIGURE 7

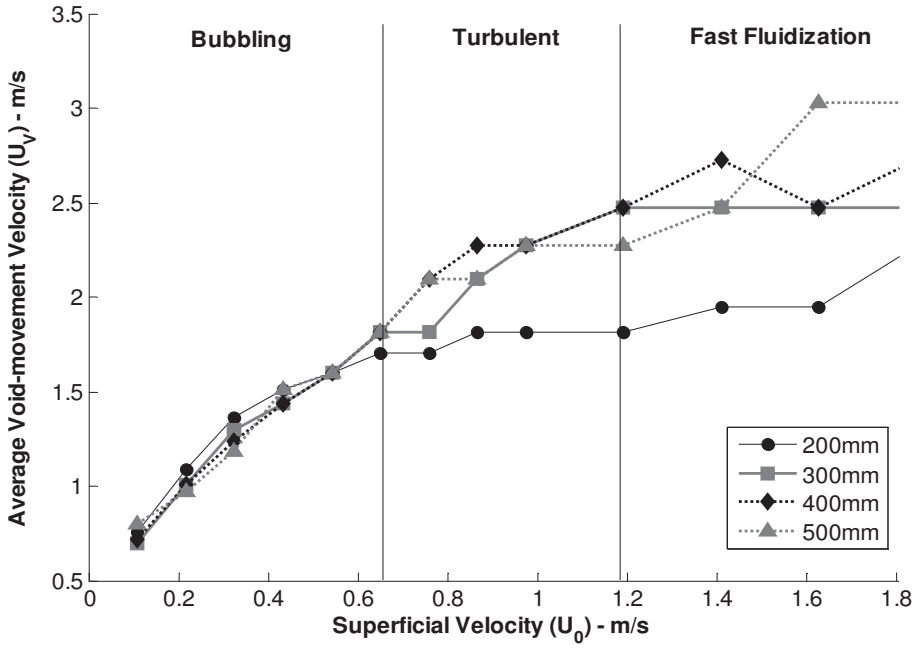
Bubbling
Turbulent
Fast Fluidization
Average Void-movement Velocity (U_v) - m/s
Superficial Velocity (U_0) - m/s
200mm
300mm
400mm
500mm
3.5
3
2.5
2
1.5
1
0.5
0
0.2
0.4
0.6
0.8
1
1.2
1.4
1.6
1.8

FIGURE 8

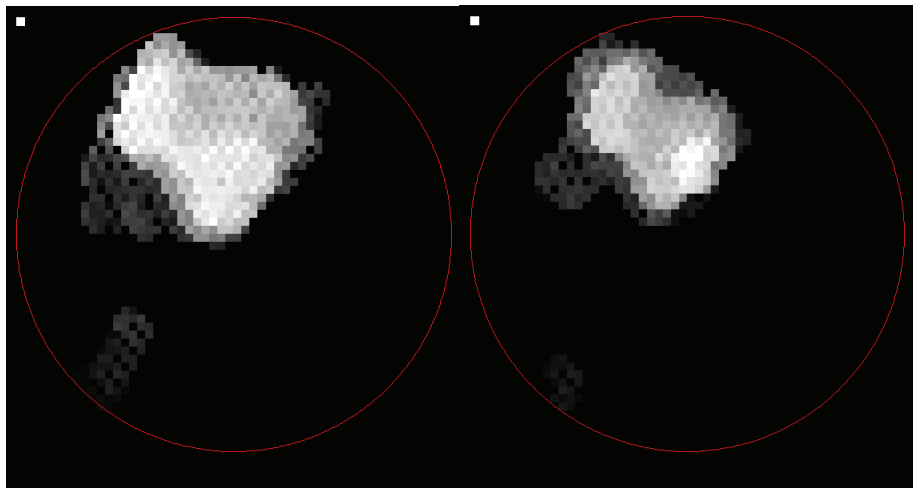

BOTTOM PLANE *TOP PLANE*

FIGURE 9

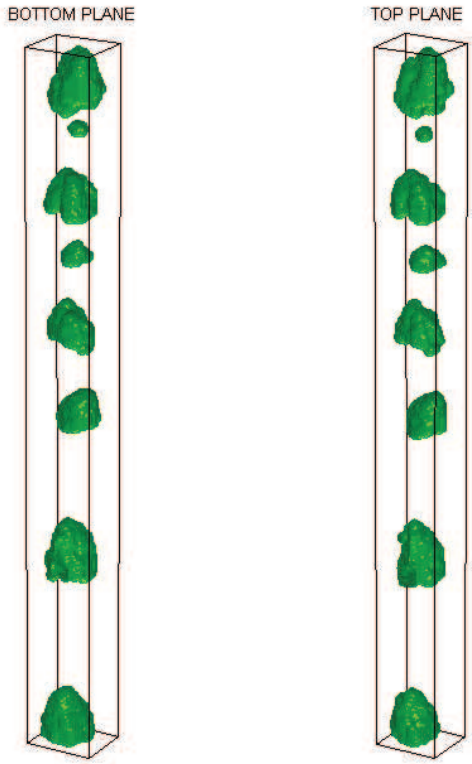

FIGURE 10

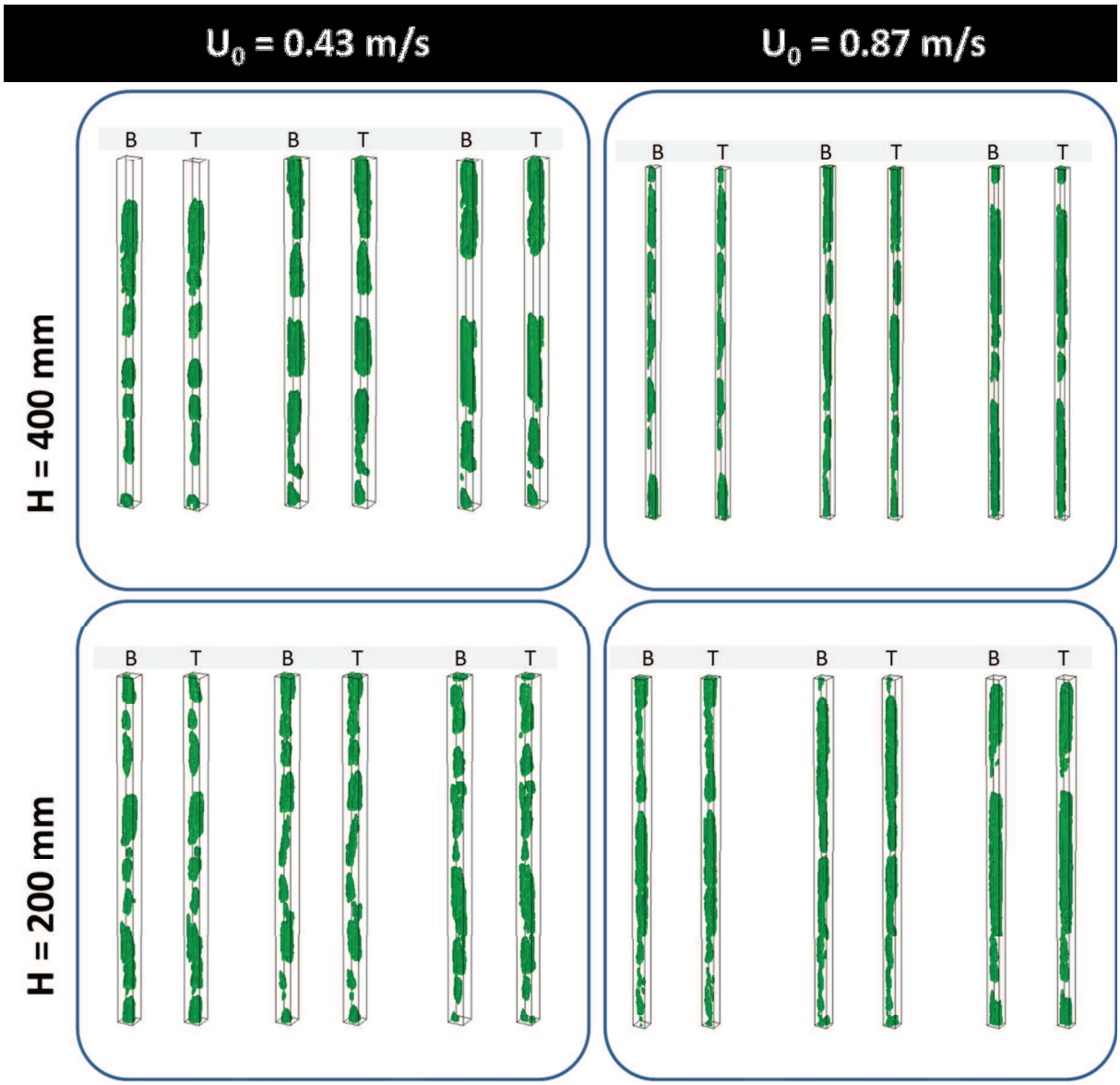

FIGURE 11

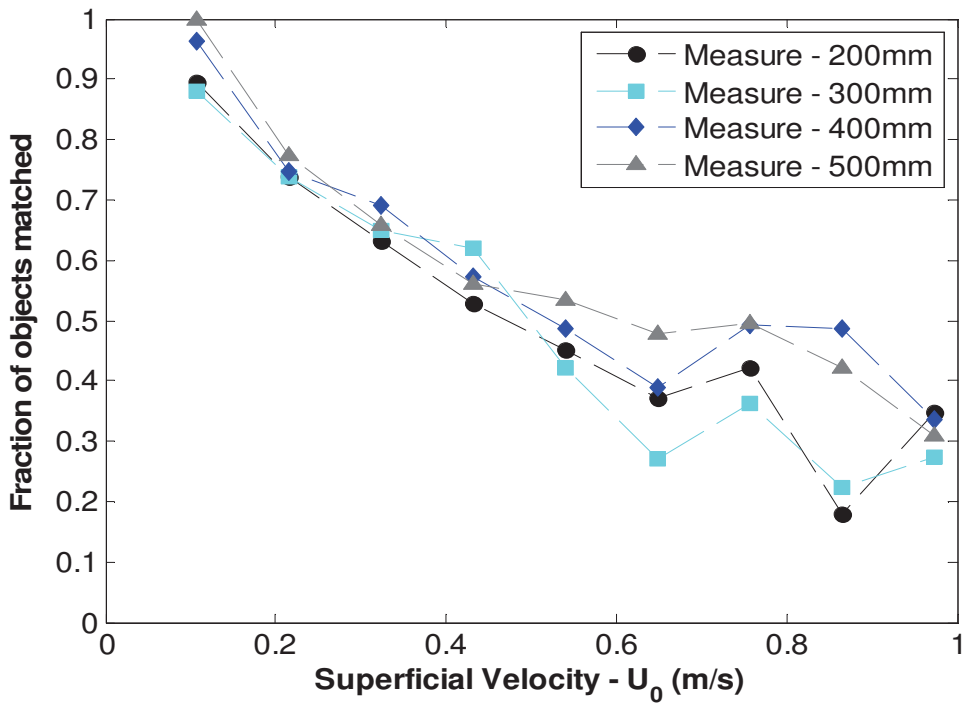
Measure - 200mm
Measure - 300mm
Measure - 400mm
Measure - 500mm
Fraction of objects matched
Superficial Velocity - U0 (m/s)
0
0.1
0.2
0.3
0.4
0.5
0.6
0.7
0.8
0.9
1
0
0.2
0.4
0.6
0.8
1

FIGURE 12

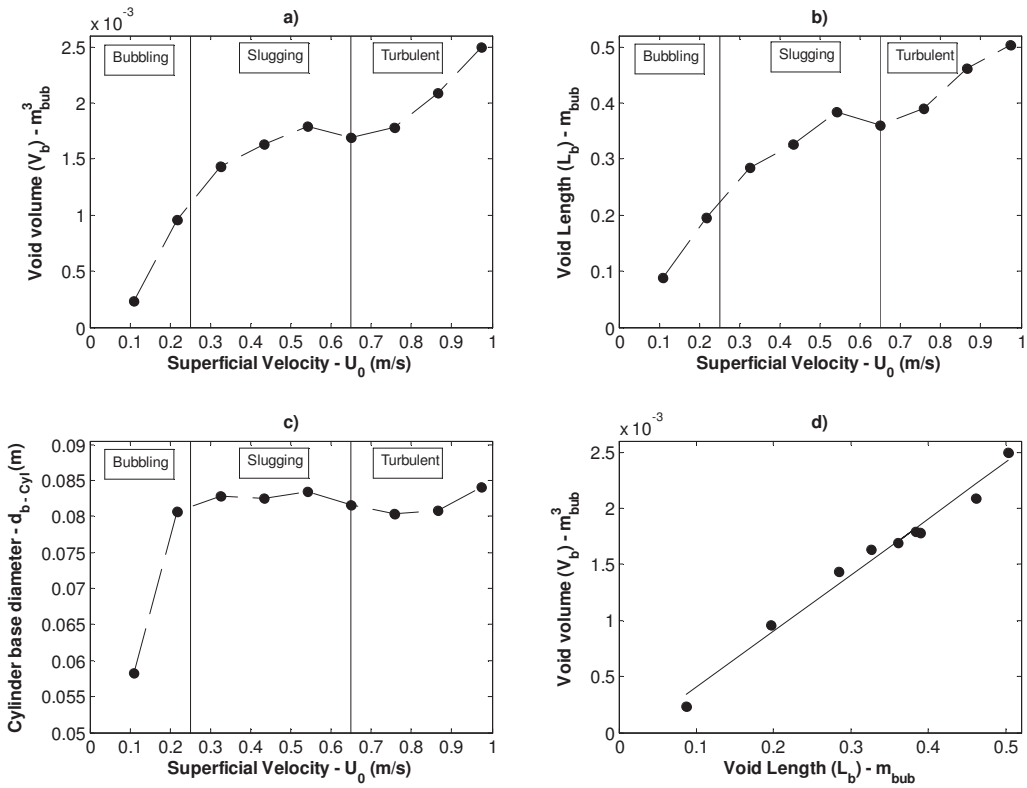
a)
x 10^-3
Bubbling
Slugging
Turbulent
Void volume (V_b) - m^3_bub
Superficial Velocity - U_0 (m/s)
b)
Bubbling
Slugging
Turbulent
Void Length (L_b) - m_bub
Superficial Velocity - U_0 (m/s)
c)
Bubbling
Slugging
Turbulent
Cylinder base diameter - d_b - Cyl (m)
Superficial Velocity - U_0 (m/s)
d)
x 10^-3
Void volume (V_b) - m^3_bub
Void Length (L_b) - m_bub

FIGURE 13

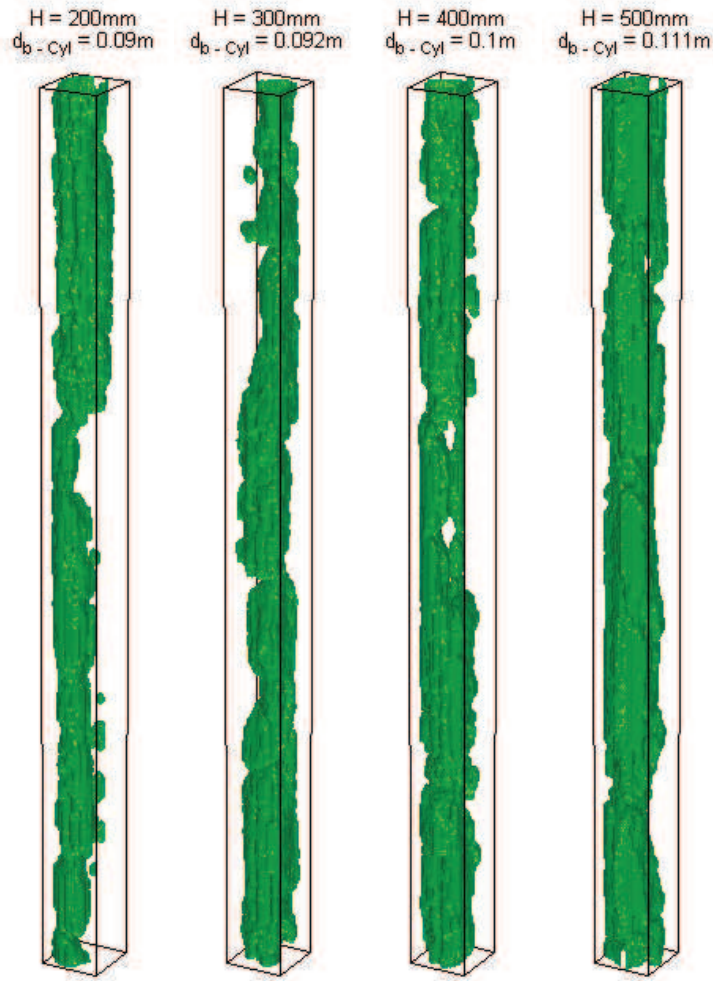
H = 200mm
$d_{b\text{ - }Cyl}$ = 0.09m
H = 300mm
$d_{b\text{ - }Cyl}$ = 0.092m
H = 400mm
$d_{b\text{ - }Cyl}$ = 0.1m
H = 500mm
$d_{b\text{ - }Cyl}$ = 0.111m

FIGURE 14

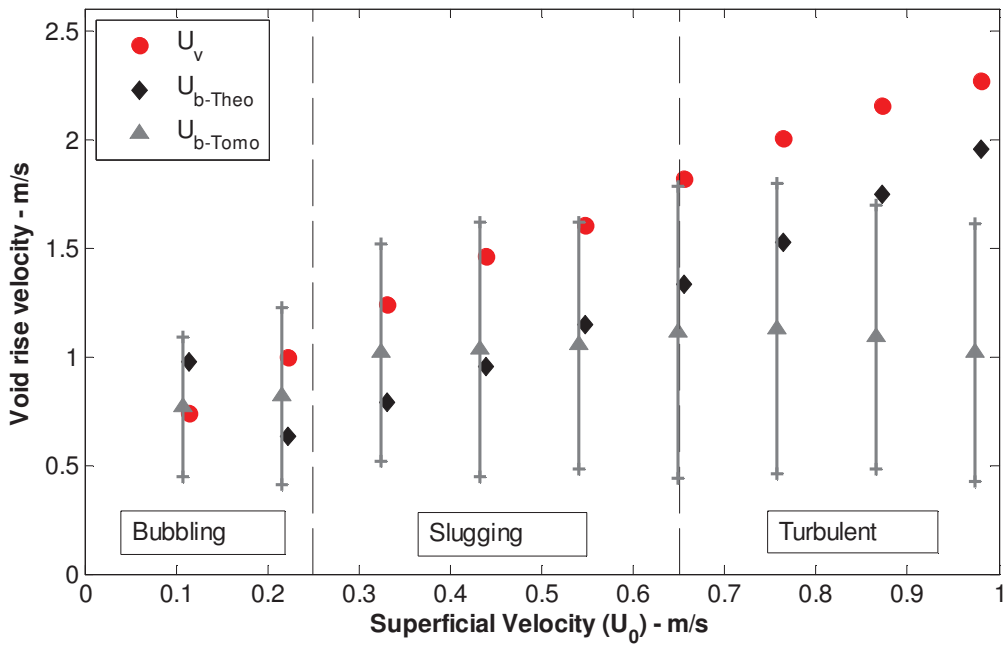
Void rise velocity - m/s
Superficial Velocity (U_0) - m/s
U_v
$U_{b\text{-}Theo}$
$U_{b\text{-}Tomo}$
Bubbling
Slugging
Turbulent
0
0.5
1
1.5
2
2.5
0.1
0.2
0.3
0.4
0.5
0.6
0.7
0.8
0.9

FIGURE 15